CrossMark

Control model and the experimental study on the ultrasonic vibration-assisted electrolytic in-process dressing internal grinding

Bo Zhao[1] · XiaoFeng Jia[1] · Fan Chen[1] · XiaoBo Wang[1]

Abstract Based on the ultrasonic vibration technology and the electrochemical principle, the ultrasonic vibration-assisted electrolytic in-process dressing internal (UAEI) grinding is realized on the vertical machining center. The mathematical control model of the UAEI grinding is established to maintain the protrusion height of abrasive grains. Simulations and fittings show that the average current is positively associated with the increase of ultrasonic frequency, grinding speed or workpiece speed, and the decrease of grinding ratio. Concrete control schemes are made by adjusting the controllable parameters. The objective judgments are obtained by comparing the experimental results under different processing conditions. The experimental results show that the surface roughness of workpiece can research 0.0487 μm, the grinding force ratio maintains at relatively stable level, topography of oxide layer presents uniform-distributed cavities, and surface micro-topography of workpiece becomes smoother with the processing parameters determined by the control model of the UAEI grinding, proving the validity of this control model of the UAEI grinding.

Keywords Ultrasonic vibration-assisted electrolytic in-process dressing internal (UAEI) grinding · Grinding force ratio · Surface roughness · Oxide layer · Control model

1 Introduction

Structural ceramics possess excellent physical and mechanical properties, such as high strength, high hardness, and high heat-resistance [1]. They are widely used in electronic optics, instrument, and aerospace and may replace hard metals widely used for wear- and corrosion-protection [2]. Various traditional methods have been proposed for machining the engineering ceramics. Kapustina and Bykova [3, 4] investigated grinding of ceramic components with free abrasive and with bonded abrasive. Piskunov and Korolev [5] developed a novel ceramic machining process named polishing, which is similar to grinding processes, to remove surface defects and micro-cracks after grinding and achieve a high surface quality. Ramesh, Yeo, Gowri, and Zhou [6] reported the viability of the super high-speed grinding technique for processing structural ceramics and analyzed the effects of the grinding parameters on the machined parts.

Compared to other traditional methods, ultrasonic-assisted grinding (UAG) and electrolytic in-process dressing (ELID) grinding display superior performance in manufacturing ceramic parts, respectively. Zaitsev, Nikitkov, and Buturovich [7] recommended the application of radial ultrasonic shear vibrations with frequency of 23.5 kHz and amplitude of 6 μm for high-productivity, defect-free grinding of Ceramics on disks of the AChK80×3 × 3 ASV80/63 Ml-100 type. Azarhoushang and Tawakoli [8] invented a novel ultrasonic unit for grinding of ceramic matrix composites. Ding et al. [9] experimentally studied the matching performance of grinding and vibration parameters in UAG of SiC ceramics and showed that the UAG technique is suitable for machining the ceramics, with lower grinding force and workpiece surface roughness, and reduced workpiece

✉ XiaoFeng Jia
59960478@qq.com

1 School of Mechanical and Power Engineering, Henan Polytechnic University, Jiaozuo 454000, China

⚫ Springer

surface profile wave height. Yan, Zhao, and Liu [10] investigated the ultraprecision surface finishing of nano-ZrO_2 ceramics using two-dimensional ultrasonic-assisted grinding. Their experimental results showed that the surface quality after two-dimensional ultrasonic-assisted grinding was superior to that two-dimensional ultrasonic-assisted grinding could significantly improve surface quality compared to diamond grinding and is easier to employ ductile grinding mode. Wei, Zhao, Jing, and Liu [11] machined engineering ceramics including Al_2O_3 ceramics, ZTA ceramics, Nano-Si_3N_4 ceramics, and Self-Si_3N_4 ceramics by rotary ultrasonic grinding machining and put forward a new evaluation parameter to evaluate the characteristics of micro-cracks. Mamalis, Kundrak, Gyani, and Horvath [12] reported a precision grinding of brittle ceramics using an electrochemically dressed wheel. Kim and Lee [13] proposed an optimum in-process electrolytic dressing (ELID) system for mirror-like grinding of fine ceramics with a metal bonded diamond wheel. Zhang, Ohmori, Marinescu, and Kato [14] compared the ELID and rotary dresser and revealed superiority of ELID grinding on the surface roughness and other surface characteristics.

However, these traditional ceramic processing methods also have their own drawbacks, such as complex set of steps, greatly difficulty in processing, poor efficiency and high processing costs [15]. Hybrid machining processes (HMPs) are drawing considerable attention from manufacturing community to meet the challenges of rigorous surface quality and high production rates. Lian et al. [16] proposed a new method called electrophoretically assisted micro-ultrasonic machining (EPAMUSM) based on micro-ultrasonic machining (MUSM) and electrorheological fluid assistance process and showed that with the appropriate processing parameters, EPAMUSM can improve machining accuracy and efficiency. Dubey, Shan, and Jain [17] presented the experimental findings in controlling the surface micro-profile and correcting out-of-roundness (OR) of the electro-chemical honing (ECH), which is a hybrid electrolytic micro-finishing technology characterized by a distinct coupling of electrochemical machining and honing actions to provide controlled functional surface generation and fast material removal capabilities in a single operation.

For the sake of achieving mirror internal surface of structural ceramics, a technique of ultrasonic vibration-assisted electrolytic in-process dressing internal (UAEI) grinding is proposed in this paper and is realized in the vertical machining center. Figure 1 shows the schematic of UAEI grinding. The cast iron bonded diamond grinding wheel and the copper cathode are treated as anode and cathode, respectively, and the electrolytic grinding fluid is provided persistently between electrodes during process. In actual composite grinding process, mixture film named oxide layer hatches on grinding wheel surface after electrical discharge
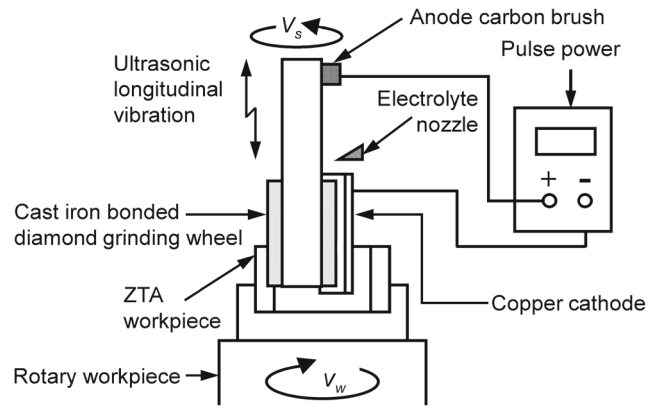
Fig. 1 Schematic illustration of UAEI

machining (EDM) dressing and UAEI pre-dressing process [18]. This mixture film is the core of precision and ultra-precision machining, which integrates grinding, lapping, and polishing into a whole [19]. The status and roles of oxide layer vary in different processing conditions. The main roles of oxide layer are to inhibit excessive electrolytic, hold free abrasive grains, and polish workpiece [20]. Finding optimal control strategies of UAEI grinding can guarantee the production efficiency and optimal surface quality and realize the high efficiency of ultra-precision mirror process.

2 Control model of UAEI grinding

2.1 Control target of UAEI grinding

UAEI grinding is a new precision machining technology that complements ultrasonic vibration grinding and ELID grinding with their respective advantages to keep grinding wheel keep at good condition. It transforms the metal bond into metal oxide by anodic dissolution effect and keeps the sharpness of abrasive grains and their protruding height well distributed. Abrasive grains vibrate in a high frequency with ultrasonic vibration. Thus, the control target is keeping constant grain protrusion height, that is to say, keeping the abrasive wear and metal bond removal heights equal.

Abrasive wear of grinding wheel can be divided into abrasive wearing, broken wearing and shedding [21]. The wheel wear stage can be divided into initial, normal, and sharp wearing stages in grinding process [22]. The abrasive grains can be easily broken and pull out at the initial wearing stage, generate abrasion wearing at the normal wearing stage, and a lot of cracks on metal bond and pull out at the sharp wearing stage. The grinding wheel can timely acquire contactless truing and keep good cutting ability, ensuring that wheel is always at normal wear stage in UAEI dynamic

grinding process. The metal bond removal rate of electrolysis is determined by Faraday's law and mainly related to electrolytic current and effective electrolytic time.

2.2 Mathematical Control Model of UAEI Grinding

Based on the control target, reasonable hypotheses were given to build a mathematical model of process control for UAEI grinding. Table 1 lists the related variables and symbols and the hypotheses are as follows:

(1) The abrasive grains are aligned and evenly distributed inside the metal bond. To simplify the calculation, the abrasive grains are treated as spherical particles. Abrasion wearing is generated when grain protrusion height exceeds the half of grain diameter.

(2) Oxide layer is eliminated fast in the dynamic grinding process and the grain protrusion height is kept constant. The effects of lapping and polishing of oxide layer are weak.

(3) The grain protrusion height (a) is uniform distributed. And the distribution density function of grain protrusion height ($f(a)$) can be given by Eq. 1

$$f(a) = \begin{cases} \frac{1}{a_{max}} \left(0 < a < a_{max} \leq \frac{2d_g}{3} \right) \\ 0 \end{cases} \tag{1}$$

The probability of grain protrusion height less than $x(P(a < x))$ can be obtained by Eq. 2

$$P(a < x) = \int_0^x \frac{1}{a_{max}} \mathrm{d}x = \frac{x}{a_{max}} \tag{2}$$

The probability of abrasive grains dominated by abrasion wearing ($P(a \geq d_g/2)$) is expressed as

$$P\left(a \geq \frac{d_g}{2}\right) = 1 - P\left(a < \frac{d_g}{2}\right) = \frac{1}{4} \tag{3}$$

The single grain volume (v_g) is

$$v_g = \frac{\pi d_g^3}{6} \tag{4}$$

The abrasive grain number per unit volume (N_v) is

$$N_v = \frac{\kappa}{v_g} \tag{5}$$

The average cross-sectional area of abrasive grain (A_m) is

$$A_m = \frac{\pi d_g^2}{6} \tag{6}$$

The abrasive grain number per unit area (N_m) can be expressed as [23]

$$N_m = N_v^{\frac{2}{3}} \tag{7}$$

Table 1 Variables and parameters applied in research

Variables	Nomenclature
A	Ultrasonic amplitude (m)
A_m	Average cross-sectional area of abrasive grain (m^2)
a	Grain protrusion height (m)
a_0	Indentation feature size (m)
a_{gc}	critical grinding depth of single grain (m)
b	Grinding wheel width (m)
D	Diameter of grinding wheel (m)
d_g	Diameter of abrasive grain (m)
C_l	transverse crack length (m)
C_h	transverse crack depth (m)
F	Faraday constant (c/mol)
$f(a)$	Distribution density function of grain protrusion height
G	Grinding ratio
I_a	Average current of electrolytic system (A)
I_{amax}	Maximum allowed average current of electrolytic system (A)
I_p	Peak current of electrolytic system (A)
K_{Ic}	Static fracture toughness of ZTA containing 15 % ZrO$_2$ (MPa.m$^{1/2}$)
K_{Id}	Dynamic fracture toughness of ZTA containing 15 % ZrO$_2$ (MPa.m$^{1/2}$)
L	Length of single grain travels in grinding zone during one vibration cycle (m)
n	Valence of iron ion
H_v	Vickers hardness of ceramic material (GPa)
H_{v0}	Vickers hardness of ZTA containing 15 % ZrO$_2$(GPa)
M	Atomic weight of metal bond (56)
M_b	Removal quantity of metal bond
N	Number of dynamic grinding grains generated abrasion wearing in grinding zone
N_h	Number of abrasion wear grains (m^{-2})
N_m	Abrasive grain number per unit area (m^{-2})
N_v	Abrasive grain number per unit volume (m^{-3})
P	Indenter load (N)
P_m	Critical load (N)
P_m^*	Dynamic critical load (N)
$P(a < x)$	Probability of grain protrusion height less than x
$P(a > d_g/2)$	Probability of abrasive grains dominated by abrasion wearing
P_n	Positive pressure of abrasive grain (N)
R_c	Duty ratio of electrolytic system
S_1	Removing cross-section area formed by plastic deformation per single grain (m^2)
S_2	Removing cross-section area formed by brittle fracture per single grain (m^2)
T	Movement periodicity of single grain (s)
V	Material removal volume by single grain
V_b	Metal bond removal volume (m^3/s)
V_g	Wear volume of abrasive grains dominated by abrasion wear per unit time (m^3/s)

Table 1 (continued)

Variables	Nomenclature
V_w	Material removal volume per unit time (m^3/s)
V_s	Wheel wear volume per unit time (m^3/s)
v_g	Single grain volume (m^3)
v_s	Grinding wheel speed (m/s)
v_w	Workpiece speed (m/s)
ZTA	zirconia-toughened alumina
γ	Cross-section area ratio of metal bond
κ	Volume ratio of abrasive grain
η	Current efficiency of electrolytic system
λ_0	Comprehensive coefficient related to Vickers hardness indentation
ζ	Vickers indenter geometrical factor
ρ_b	Density of metal bond (Kg/m^3)
ρ_g	Density of abrasive grain
ω	Cross-section area ratio of abrasive grain (Kg/m^3)
τ	Percentage of grain (Kg/m^3)
$\omega_0 t$	Phase Angle

The number of abrasion wearing grains in a unit area (N_h) is

$$N_h = N_m.P\left(a \geq \frac{d_g}{2}\right) = \frac{1}{4}.N_m \tag{8}$$

The number of dynamic grinding grains generated abrasion wearing per unit time in the grinding zone (N) can be determined by the following equation

$$N = N_h b(v_s + v_w) \tag{9}$$

The cross-sectional area ratio of abrasive grain (ω) is

$$\omega = A_m.N_m \tag{10}$$

The cross-section area ratio of metal bond (γ) is

$$\gamma = 1 - \omega \tag{11}$$

The ceramic material removal mode can be divided into plastic removal mode and brittle removal mode. The indentation experiment by Lawn and Wilshaw [24] showed that the indenters cause plastic flowed into ceramic surface at a slow speed under the action of the indenter load (P). After unloading, the ceramic surface remained indentation without any crack, as shown in Fig. 2. These results suggest that brittle material undergoes plastic deformation under certain conditions. When the indentation is generated by the formation of the material microscopic plastic flow, the indenter load (P) can be expressed by Eq. 12 [25, 26].

$$P = \zeta.H_v.a_0^2 \tag{12}$$
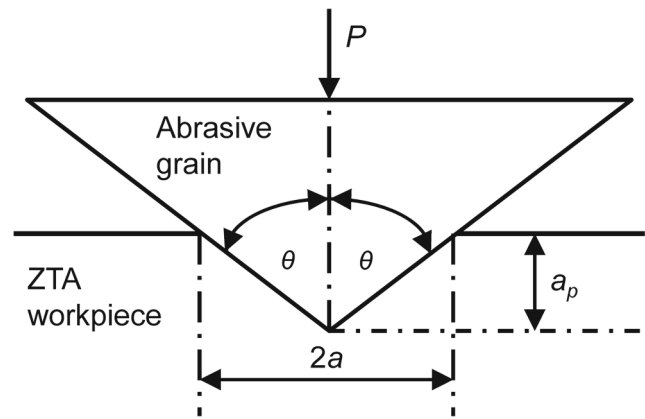

Fig. 2 Indentation model of abrasive grain

When the indenter load (P) continues to increase, a radial crack will be generated and extended under the plastic deformation zone, as shown in Fig. 3. The local plastic deformation of material indentation and stress field of radial crack will cause transverse cracks during the unloading process. When the extend conditions of transverse cracks are met, transverse cracks will extend forward and toward the surface. The critical load, which leads to crack propagation (P^*), can be expressed as [22]

$$P^* = \lambda_0 K_{Ic}\left(\frac{K_{Ic}}{H_v}\right)^3 \tag{13}$$

The indentation feature size (a_0) can be expressed as $a_0 = a_p.\tan\theta$. The positive pressure of abrasive grain (P_n) can be obtained from Eq. 14.

$$P_n = \frac{1}{2}.\zeta.H_v.a_p^2.\tan^2\theta \tag{14}$$

The big shock action occurred due to the instant contact of abrasive grain with workpiece in actual grinding process. The static fracture toughness (K_{Ic}) should be replaced with
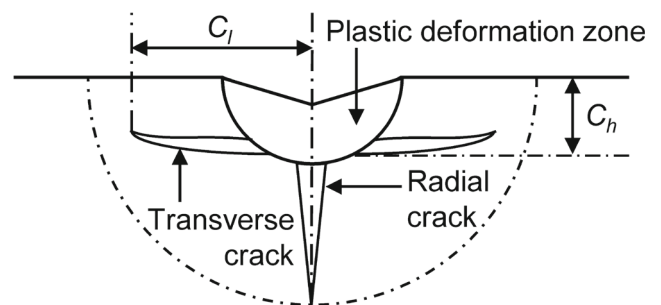
Fig. 3 Removal model of ductile fracture material

the dynamic fracture toughness (K_{Id}). Thus, the dynamic critical load (P_m^*) can be shown as

$$P_m^* = \lambda_0 K_{Id} \left(\frac{K_{Id}}{H_v} \right)^3 \tag{15}$$

The K_{Ic} of ZTA containing 15 % ZrO_2 is 9.4MPa.m$^{1/2}$ [27]. Sairam and Clifton [28] conducted plate impact experiment to research the dynamic fracture law and showed that the K_{Id} is about thirty percent of the K_{Ic}. Therefore, the K_{Id} of ZTA containing 15 % ZrO_2 is 2.8MPa.m$^{1/2}$.

Combining of Eqs. 14 and 15, the critical grinding depth of single grain (a_{gc}) can be obtained using the Eq. 16.

$$a_{gc} = \sqrt{ \frac{2\lambda_0}{\zeta \tan^2 \theta} (\frac{K_{Id}}{H_{v0}})^2 } \tag{16}$$

Whether the grinding surface is formed by plastic deformation or brittle fracture mainly depends upon the single grain cutting thickness (a_p) and the critical cutting thickness (a_{gc}). When the single grain cutting thicknesss is equal to or less than the critical cutting thickness ($a_p \leq a_{gc}$), the grinding surface is formed by microscopic plastic deformation, and the removal shape is triquetrous curvilinear cylindrical in each vibration cycle. The removing cross-section area formed by plastic deformation per single grain (S_1) can be expressed as

$$S_1 = a_p^2 \tan \theta \tag{17}$$

When the critical cutting thickness is less than the single grain cutting thickness ($a_p > a_{gc}$), the grinding surface is formed by both microscopic plastic deformation and brittle fracture. The transverse crack length (C_l) and transverse crack depth (C_h) can be expressed as Eqs. 18 and 19, respectively [29].

$$C_l = \zeta_1 \left(\frac{P_n}{K_{Ic}} \right)^{\frac{3}{4}} \tag{18}$$

$$C_h = \zeta_2 \left(\frac{P_n}{H_v} \right)^{\frac{1}{2}} \tag{19}$$

where ζ_1 and ζ_2 are the proportionality coefficient, independent of the material/indenter system. The removing cross-section area formed by brittle fracture per single grain (S_2) in brittle removal process can be expressed as

$$S_2 = 2.C_l.C_h \tag{20}$$

Based on the characteristics of simple harmonic motion, during one vibration cycle, the length of single grain travels in grinding zone (L) shown in Fig. 4 can be expressed as

$$L = \int_0^T \sqrt{(v_s + v_w)^2 + (A\omega_0 \cos \omega_0 t)^2} \, dt \tag{21}$$

During one vibration cycle, the material removal volume by single grain (V) can be expressed by Eq. 22 and material removal volume per unit time (V_w) can be expressed by Eq. 23

$$V = \begin{cases} a_p^2 \tan \theta \int_0^T \sqrt{(v_s + v_w)^2 + (A\omega_0 \cos \omega_0 t)^2} \, dt & (a_p \leq a_{gc}) \\ 2\zeta_1 \zeta_2 \left(\frac{P_n}{K_{Ic}} \right)^{\frac{3}{4}} \left(\frac{P_n}{H_v} \right)^{\frac{1}{2}} \int_0^T \sqrt{(v_s + v_w)^2 + (A\omega_0 \cos \omega_0 t)^2} \, dt & (a_p > a_{gc}) \end{cases} \tag{22}$$

$$V_w = \begin{cases} f.a_p^2 \tan \theta.N \int_0^{\frac{1}{f}} \sqrt{(v_s + v_w)^2 + \left[\frac{2A\pi f}{v_s+v_w} \cos \left(\frac{2\pi f t}{v_s+v_w} \right) \right]^2} \, dt & (a_p \leq a_{gc}) \\ f.2\zeta_1 \zeta_2 \left(\frac{P_n}{K_{Ic}} \right)^{\frac{3}{4}} \left(\frac{P_n}{H_v} \right)^{\frac{1}{2}}.N \int_0^{\frac{1}{f}} \sqrt{(v_s + v_w)^2 + \left[\frac{2A\pi f}{v_s+v_w} \cos \left(\frac{2\pi f t}{v_s+v_w} \right) \right]^2} \, dt & (a_p > a_{gc}) \end{cases} \tag{23}$$

Grinding ratio (G) is defined as the ratio of material removal volume per unit time (V_w) to wheel wear volume per unit time (V_s) [30].

$$G = \frac{V_w}{V_s} \tag{24}$$

Based on Eq. 3, the wear volume of abrasive grains dominated by abrasion wearing per unit time (V_g) is

$$V_g = \frac{V_s.\tau.P(a \geq \frac{d_g}{2})}{\rho_g} \tag{25}$$

According to the principle of electrochemical, the removal quantity of metal bond (M_b) can be expressed as

$$M_b = \frac{\eta M I_p R_c}{nF} \tag{26}$$

The metal bond removal volume (V_b) can be expressed as

$$V_b = \frac{\eta M I_p R_c}{nF\rho_b} \tag{27}$$

Owing to the control target of keeping abrasive wear and metal bond removal equal height, the equation can be expressed as

$$\frac{V_g}{A_m} = \frac{V_b}{\pi D b \gamma} \tag{28}$$

Above all, the average current(I_a), which is the product of peak current (I_p) and duty ratio (R_c), can be drawn by Eq. 29

$$I_a = I_p R_c = \begin{cases} \dfrac{3f\tau a_p^2 \tan\theta . b^2 (v_s+v_w).nF.\rho_b.D.(1-\omega).\sqrt[3]{\frac{36}{\pi^2}}.\kappa^{\frac{2}{3}}\int_0^{\frac{1}{f}}\sqrt{(v_s+v_w)^2+\left[\frac{2A\pi f}{v_s+v_w}\cos\left(\frac{2\pi f t}{v_s+v_w}\right)\right]^2}\,dt}{8\eta MG.\rho_g.d_g^4} & (a_p \leq a_{gc}) \\[3em] \dfrac{3f\zeta_1\zeta_2\tau\left(\frac{P_n}{K_{Ic}}\right)^{\frac{3}{4}}\left(\frac{P_n}{H_v}\right)^{\frac{1}{2}}.b^2(v_s+v_w).nF.\rho_b.D.(1-\omega).\sqrt[3]{\frac{36}{\pi^2}}.\kappa^{\frac{2}{3}}\int_0^{\frac{1}{f}}\sqrt{(v_s+v_w)^2+\left[\frac{2A\pi f}{v_s+v_w}\cos\left(\frac{2\pi f t}{v_s+v_w}\right)\right]^2}\,dt}{4\eta MG.\rho_g.d_g^4} & (a_p > a_{gc}) \end{cases}$$
(29)

2.3 Simulation and analysis of mathematical control model of UAEI grinding

The key point of control strategy is to make clear the correlations of influence factors (f, v_s, v_w, G) and the average current (I_a). In order to explore the relationship between the average current and influence factors, simulation analyses of above Eq. 29 were carried out by Wolfram Mathematica9.0 and MATLAB.The simulation parameters are summarized in Table 2. The data of average current with different ultrasonic frequency, grinding ratio, wheel speed, or workpiece speed were obtained by Wolfram Mathematica9.0 and were fitted using MATLAB regression. Observing the Eq. 29, the influence of ultrasonic frequency, grinding ratio, wheel speed and workpiece speed on the average current is consistent in both cases of $a_p \leq a_{gc}$ and $a_p > a_{gc}$.Thus, adopting the function of $a_p \leq a_{gc}$ simulates the effect trends.

The exponential models are proposed to fit the curves of average current versus ultrasonic frequency or grinding ratio, separately, and obtaining good fitting effect. The fitting functions are expressed by the Eqs. 30,31.

$$f(x_1) = 5.513e^{(-1.443 \times 10^{-6})x_1} + 3.345e^{(2.367 \times 10^{-6})x_1}$$
(30)

$$f(x_2) = 36.31e^{-0.001216x_2} + 11.87e^{-0.0002032x_2}$$
(31)

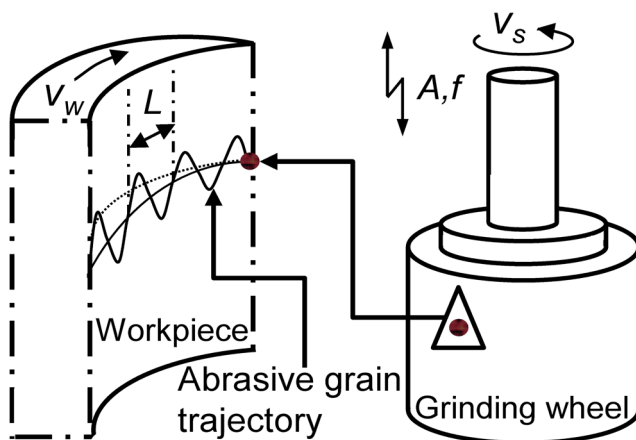The polynomial models are brought up on fitting the curves of average current versus wheel speed or workpiece speed, separately. The fitting functions are expressed by the Eqs. 32,33.

$$f(x_3) = 0.4553x_3^2 + 0.1336x_3 + 0.2766$$
(32)

$$f(x_4) = 3.91x_4 + 7.784$$
(33)

According to Fig. 5, the positive correlation between average current (I_a) and ultrasonic frequency (f), wheel speed (v_s) or workpiece speed (v_w), and the negative correlation between average current (I_a) and grinding ratio (G) were presented.

To illustrate, Fig. 6 shows the concrete flow chart of the control strategy. Firstly, determine material that needs to

Table 2 Simulation parameters

Parameters	Values
Abrasive diameter d_g	5×10^{-5}
Abrasive half-apex angle $\theta(°)$	52
Comprehensive coefficient related to Vickers hardness indention	21684.9
current efficiency η	0.6
Diamond density ρ_g(kg/m^3)	3510
Dynamic fracture toughness K_{Id}(Mpa.m$^{1/2}$)	2.8 [28]
Faraday constant F(c/mol)	96485
Grinding depth a_p(m)	3×10^{-6}
Grinding grain of cross-sectional area ratio ω	0.32
Metal bond atomic weight M	56
Metal bond density ρ_b(kg/m^3)	7800
Percentage of grain τ(kg/m^3)	880
Pulse power duty ratio R_c	0.5
Reactive ion valence n	3
Static fracture toughness K_{Ic}(Mpa.m$^{1/2}$)	9.4 [27]
Ultrasonic amplitude $A(m)$	8×10^{-6}
Ultrasonic frequency F(kHz)	35
Vickers hardness H_v(GPa)	16.9
Vickers indenter geometrical factor	1.8544
Wheel diameter D (m)	0.025
Wheel speed v_s (m/s)	4.2
Workpiece speed v_w (m/s)	0.28
Wheel width b(m)	0.017

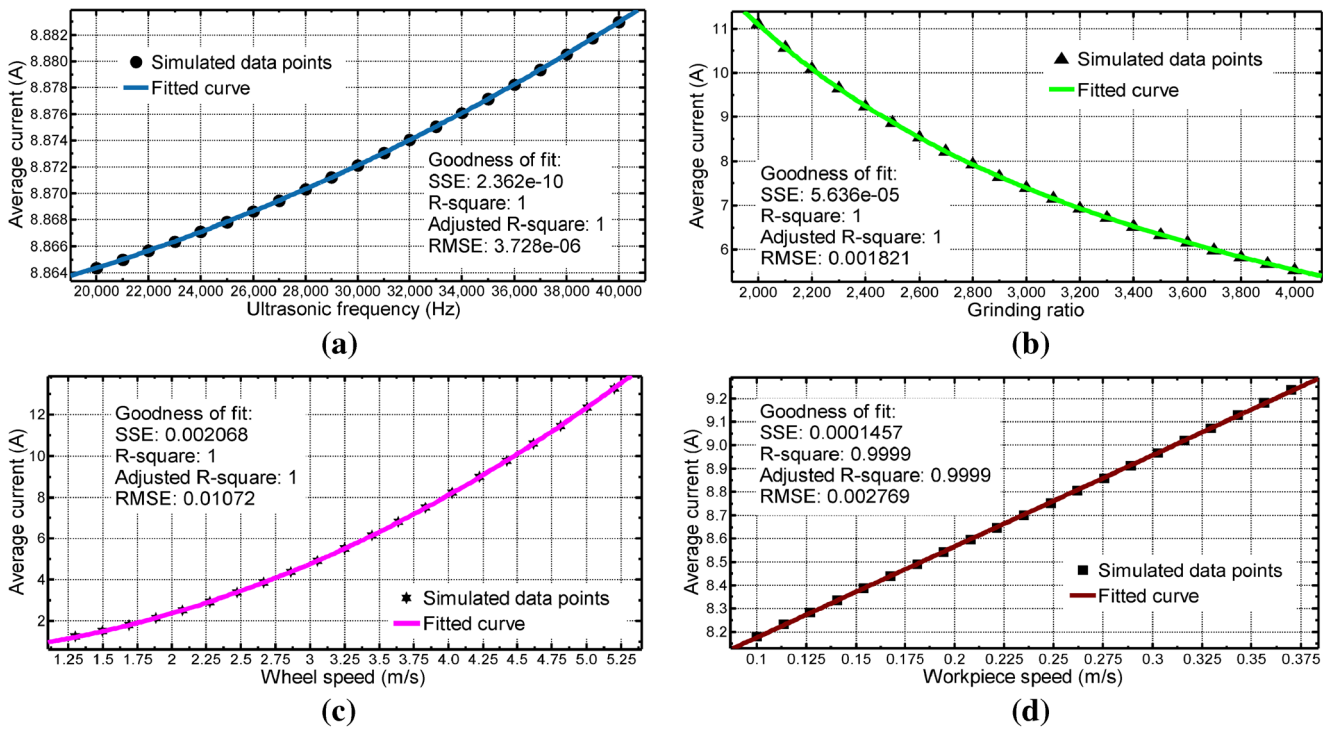**Fig. 4** Abrasive grain trajectory for UAEI grinding

Fig. 5 Correlation trend simulation of ultrasonic frequency, grinding ratio, wheel speed and workpiece speed on average current

be processed and the values of dynamic fracture toughness (K_{Id}) and Vickers hardness (H_v). Secondly, select the suitable grinding wheel parameters and processing parameters base on the workpiece material, rigidity and manufacturing requirement. Thirdly, confirm the grinding ratio according

Fig. 6 Concrete flow charts of the control strategy

to the experimental methods. Fourthly, calculate the critical grinding depth (a_{gc}) of single grain processing using Eq. 16. Fifthly, select the matching UAEI grinding control model according to actual grinding depth obtained by Eq. 29. Lastly, adjust the appropriate electrical parameters. If the average current (I_a) goes beyond its maximum allowed (I_{amax}), skip to the next iteration of the loop by adjusting the processing parameters (f, v_s, v_w).
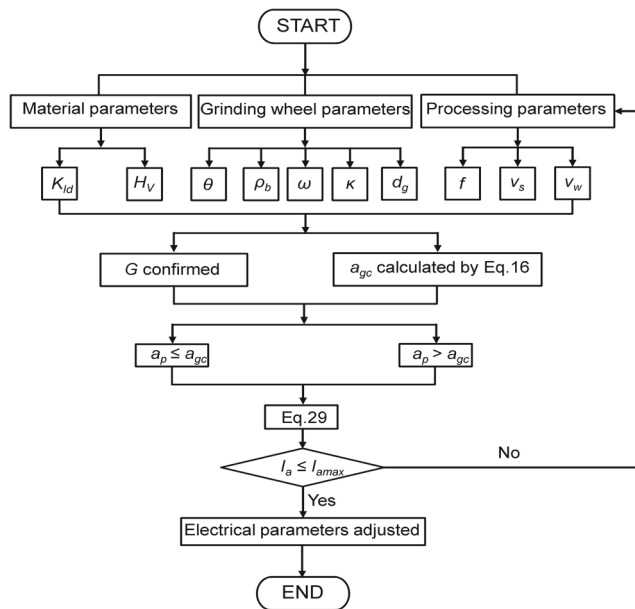
3 Experimental demonstrations of UAEI grinding mathematical control model

3.1 Experimental setup

The experimental setup was composed of four parts: ultrasonic machining system, three axis vertical machining center, rotary table, and on-line electrolytic system. The ultrasonic machining system has an ultrasonic wireless transmission and an ultrasonic generator. The three-axis vertical machining center (VMC 850E, Shenyang, China) has fitted with ultrasonic machining system and on-line electrolytic system. The actual experimental setup is shown in Fig. 7. The grinding force was measured by dynamometer (9257B, Kistler, Switzerland). The surface roughness of workpieces was measured by the roughness
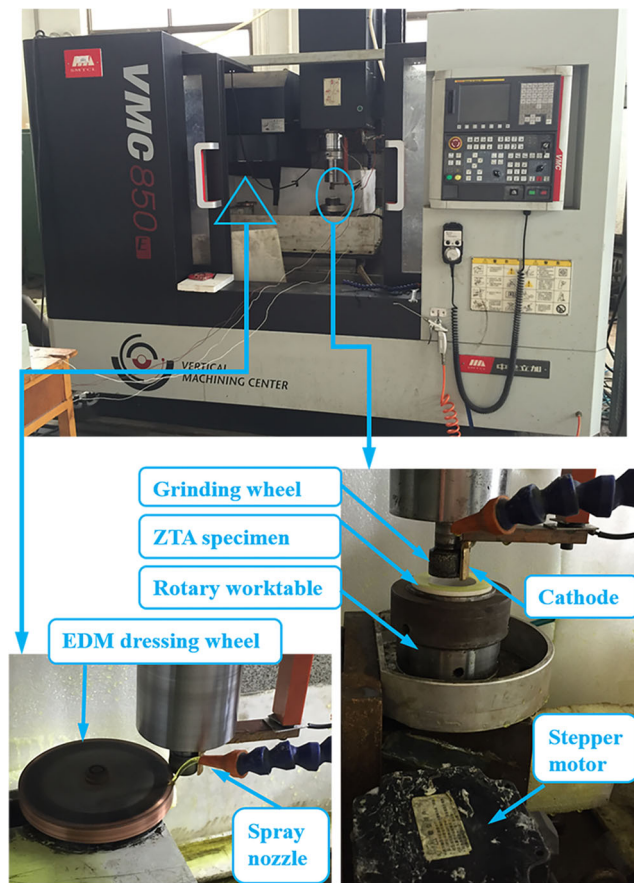
Fig. 7 Actual experimental setups of UAEI grinding

testers (Surtronic 3+ and Talysurf CCI6000, Taylor/Hobson, England). Surface topographies were measured by the tabletop scanning electron microscope (SH4000M, Hirox, China) at vacuum mode of high vacuum, magnification of 1.0K and accelerating voltage of 15kV. Oxide layer topographies were obtained by digital microscope (VHX-2000, Keyence, Japan).

3.2 Electrical discharge machining (EDM) dressing

The rough shaping was performed at voltage of 120V, duty ratio of 90s:10s and grinding feed of $3\mu m$ per longitudinal travel for 30min. The half precision shaping was conducted at voltage of 90V, duty ratio of 45s:45s and grinding feed of $2\ \mu m$ per longitudinal travel for 20min.The precision shaping was proceeded at voltage of 60V, duty ratio of 10s:10s and grinding feed of $2\mu m$ per longitudinal travel for 10min. After that, the radial run-out values of each measurement point were measured using a pointer micrometer until the radial run-out error met the shaping requirements of below $3\mu m$.

3.3 Ultrasonic vibration-assisted electrolytic pre-dressing

The ultrasonic vibration-assisted electrolytic pre-dressing was performed at voltage of 90V, duty ratio of 10s:5s, and wheel speed of 3200 r/min for 30min to make oxide layer thickness being about $150\mu m$.

3.4 Determine the grinding ratio at different processing conditions

The same inner diameters and surface roughness of ZTA specimens were guaranteed by precision grinding. Under the certain grinding parameters shown in the Table 3, the weights of ZTA specimens before and after every grinding process were measured using a precision balance with accuracy of 0.001g and converted to the material removal volumes. The radial wear of the wheels at five randomly distributed measurement points was measured before and after every grinding process using a precision electronic digital display micrometer. And the average values were taken as the wheel radial wear and converted to the wheel wear volumes. Before each measurement, the specimens and grinding wheels were cleaned with acetone, dried to constant weight and cooled to room temperature. The grinding ratios of three replications were calculated using Eq. 24, and the average value was taken as the grinding ratio under the certain grinding parameters.

3.5 Experimental method

The verification experiments were carried out at different grinding ratio, workpiece surface roughness, workpiece surface microstructure, and oxide layer morphology. To ensure the accuracy of the experiments, grinding ratio and grinding force were determined separately for three times and the mean values were adopted. As shown in Fig. 8, to

Table 3 Experimental conditions

Grinding method	Ultrasonic vibration-assisted electrolytic in-process dressing cut into the inner circle reverse grinding
ELID Pulse power	HDMD-IV high frequency pulse power
Grinding fluid	ELID grinding fluid
Machine tool	VMC850E
Grinding wheel	Medium-hard cast iron bond diamond wheel with a grain concentration of 100 %, a diameter of 25 mm and a width of 17 mm
Workpiece specimen	ZTA ceramic with a inner diameter of 35mm, a outer diameter of 60mm and a thickness of 20 mm

Fig. 8 surface roughness test
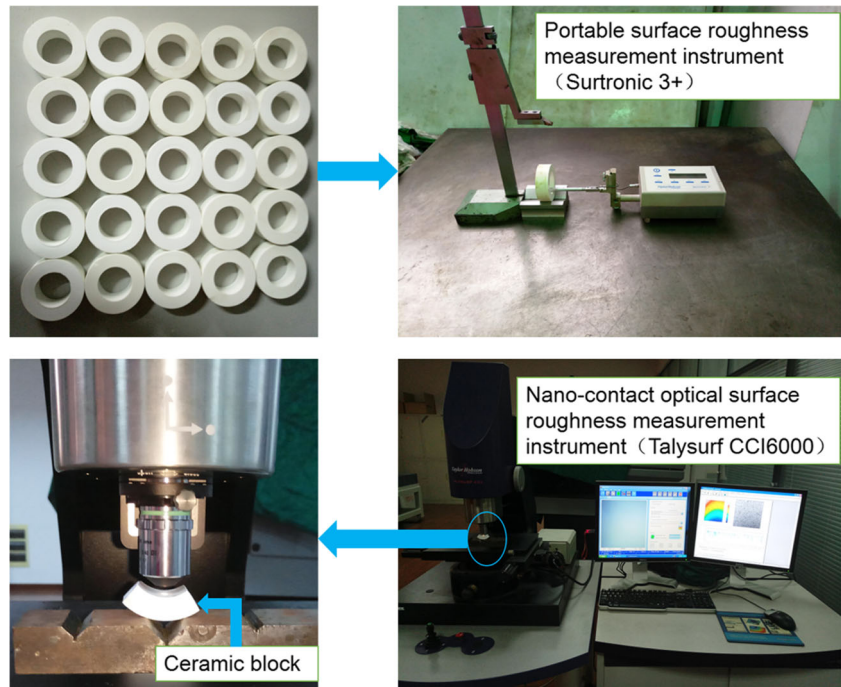
acquire the same initial roughness data, twenty-five ZTA specimens with the same inner diameters were selected for precision grinding using 280# grinding wheel. The surface roughness of each ZTA specimen was measured four times using a portable Surtronic 3+ surface roughness measurement instrument. The results showed that the roughness varied around at 0.05 μm with average of 0.0514 μm. Then, five ZTA specimens were randomly selected and cut into ceramic blocks to measure surface roughness using Talysurf CCI6000, a non-contact optical surface roughness measurement instrument. The results showed that the roughness values of the five ZTA specimens were very close to the average roughness value of 0.0514 μm; thus, the average roughness value was adopted as the initial roughness value. The remaining 20 ZTA specimens from different measurement points in time were cut into ceramic blocks and measured four times per specimen using Talysurf CCI6000 to obtain the average roughness values, which were treated as the final roughness values of each measurement point.

3.6 UAEI dynamic grinding

Two groups of processing parameters determined by the mathematical control model of UAEI grinding and two groups of specified processing parameters were adopted to process same specification ZTA ceramics by the UAEI grinding. The experimental design for verification of the mathematical control model was predicted in Table 4.

4 Experimental results and analysis

4.1 Grinding force ratio and workpiece surface roughness in grinding process

The essence of UAEI grinding is the self-sharpening behavior of abrasive grains based upon the interaction of ultrasonic vibration and electrochemical dissolution. If the effects of self-sharpening and wear could not be cancelled

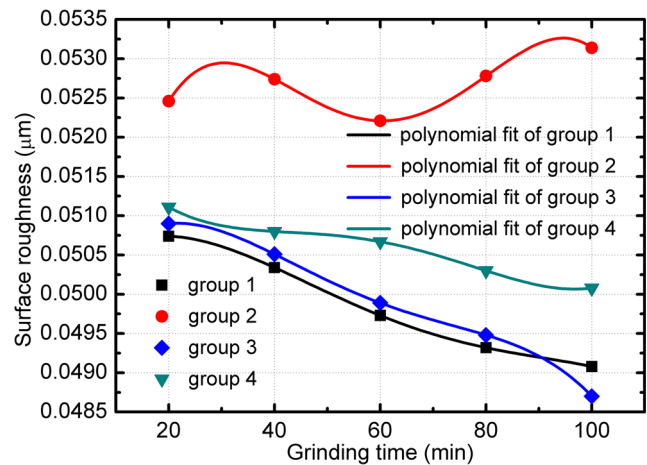**Table 4** Experimental design for verification

Group number	Grain size	Ultrasonic frequency (Hz)	Wheel speed (m/s)	Workpiece speed (m/s)	Grinding ratio	Voltage (V)	Grinding depth (m)
1	280#	35000	4	0.26	2804	60	5×10^{-6}
2	280#	35000	4	0.26	—	120	5×10^{-6}
3	W40	25000	2.6	0.3	5016	90	1×10^{-6}
4	W40	25000	2.6	0.3	—	60	1×10^{-6}
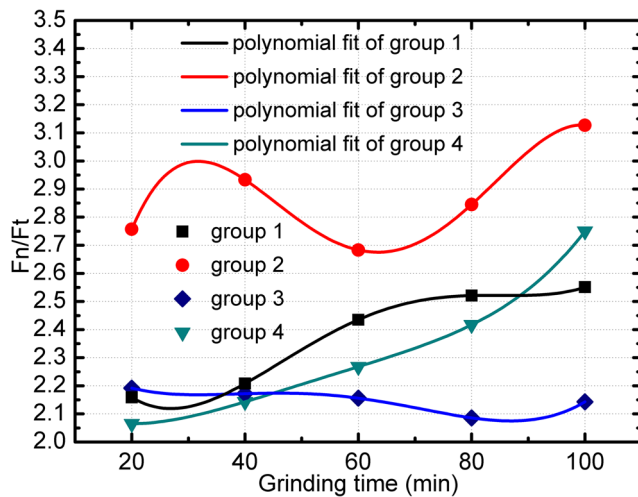
Fig. 9 Change rules of grinding force ratio over grinding time

Fig. 10 Change rules of workpiece surface roughness over grinding time

out, the normal grinding force would increase dramatically but the tangential grinding force would increase slowly. Therefore, the self-sharpening behavior of wheel in each group could be judged in terms of grinding force ratio and used to determine the effectiveness of the mathematical control model of UAEI grinding.

The trends of grinding force ratio and workpiece surface roughness with grinding time at different conditions (groups) are shown in Figs. 9 and 10, respectively. The experimental data listed in Table 5 fitted well with the polynomials. From Fig. 9, it is clear that the grinding force ratio increased at varying degrees in groups 1, 2, and 4, but slightly decreased in group 3 over time. From Fig. 10, it is clear that the workpiece surface roughness decreased to different degrees in groups 1, 3, and 4, but increased slightly in group 2 over time. These phenomena are due to the following reasons. First, the electrolytic speed of metal bond is fast and the abrasive particles on the surface of the wheel are replaced quickly under the reaction force of the workpiece, leading to unstable grinding condition in group 2. Therefore, the grinding force ratio varies greatly and the workpiece surface roughness increases in group 2. Second, metal bond removal rate and abrasive

particle mechanical wear rate achieve balance in groups 1 and 3. Consequently, the grinding force ratio changes smoothly and the workpiece surface roughness decreases slowly. Third, the ability of electrolytic in-process dressing is weak in group 4, the wear rate of abrasive grains is greater than metal bond removal rate, and blunt grains cannot detach from the wheel in time, leading to that the grinding force ratio increases with grinding force increasing. After a period of time, the effects of extrusion and scratch are enhanced, and grinding force ratio gradually is stabilized.

4.2 Surface micro topography of machined workpieces

ZTA ceramic is a hard brittle material. Under the action of external force, the crystals on the ceramic surface generate intergranular fractures or transgranular fractures and separate from the processed body, leaving a large numbers of pits on the surface and generating massive microcracks. Material removal process is a complicated process where both plastic deformation removal and brittle fracture removal occur simultaneously. Therefore, the processing condition in each group could be judged in terms of surface micro

Table 5 The experimental data of grinding force ratio and workpiece surface roughness

Grinding time (min)	Grinding force ratio of group 1	Grinding force ratio of group 2	Grinding force ratio of group 3	Grinding force ratio of group 4	Workpiece surface roughness of group 1 (μm)	Workpiece surface roughness of group 2 (μm)	Workpiece surface roughness of group 3 (μm)	Workpiece surface roughness of group 4 (μm)
20	2.159	2.757	2.192	2.065	0.05074	0.05246	0.0509	0.05111
40	2.208	2.933	2.172	2.143	0.05034	0.05274	0.05051	0.0508
60	2.435	2.683	2.156	2.268	0.04973	0.05221	0.04989	0.05067
80	2.521	2.845	2.086	2.417	0.04932	0.05278	0.04948	0.0503
100	2.551	3.127	2.143	2.75	0.04908	0.05314	0.0487	0.05008

topographies of the machined workpieces used to determine the effectiveness of the mathematical control model of UAEI grinding.
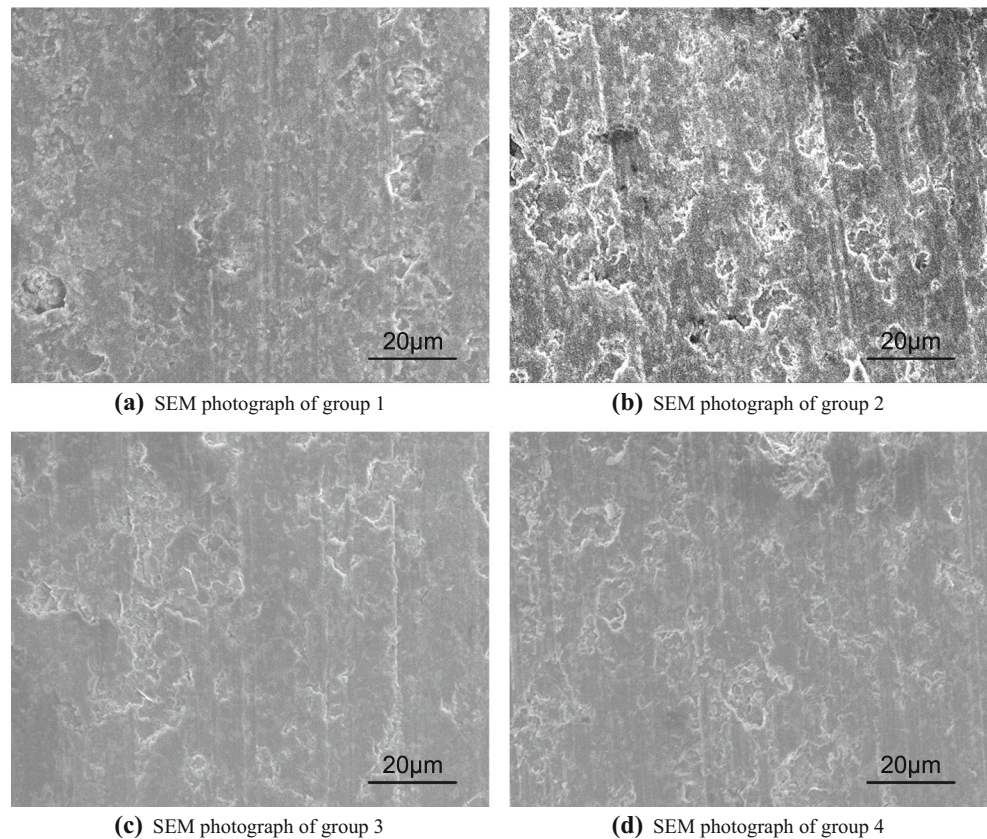
Figure 11 shows the surface morphology of the machined workpieces obtained at various processing conditions under scanning electron microscope (SEM). It clearly shows different degrees of grooves and micro grinding marks on the surface of the machined workpieces obtained at various processing conditions. Ridge crests induced by plastic deformation are obvious and tiny broken particles and squamous breaking traces can be seen on the surface of the grinding traces in group 1 and group 2, indicating that the material removal is mainly brittle fracture removal. Surface topography is relatively flat and uniform, and the grooves and pits are not obvious on the surface of the machined workpieces in group 3 and group 4, mainly because the removal of ZTA ceramic is mainly plastic removal mode under shallow grinding depth. Comprehensive comparison of the surface micro topographies of the four groups clearly proves the superiority of machining parameters determined by the mathematical control model. Among the four groups, the surface properties of group 3 are the best. The reason is that the generation and removal of oxide layer basically maintain in a balanced state under the actions of ultrasonic vibration and electrochemical reaction. Before achieving the critical grinding depth, the high frequency vibration of

wheel leads to tiny broken particles, thus avoiding the whole shedding of crystals or large area of pits induced by crack propagation. The surface of the machined workpieces in group 1 is relatively flat, but has pits. The reason is that although abrasive particles on the surface of wheel maintain self-sharpening, the actual grinding depth exceeds the critical depth and the main removal way of ZTA material is brittle fracture. The electrolytic speed in group 2 is very fast; thus, the removal rate of metal bond is larger than the wear rate of grinding wheel, leading to premature loss of abrasive grains. The decline of grinding edge density causes the deterioration of surface properties. The electrolytic speed in group 4 is very slow; thus, the removal rate of metal bond is slower than the wear rate of grinding wheel. As the result, abrasive grains cannot self-sharpen in time. In addition, grinding depth is relatively small, which enhances the squeezing and scratching between abrasive grains and workpieces. Therefore, the workpieces possess well good surface micro topography.
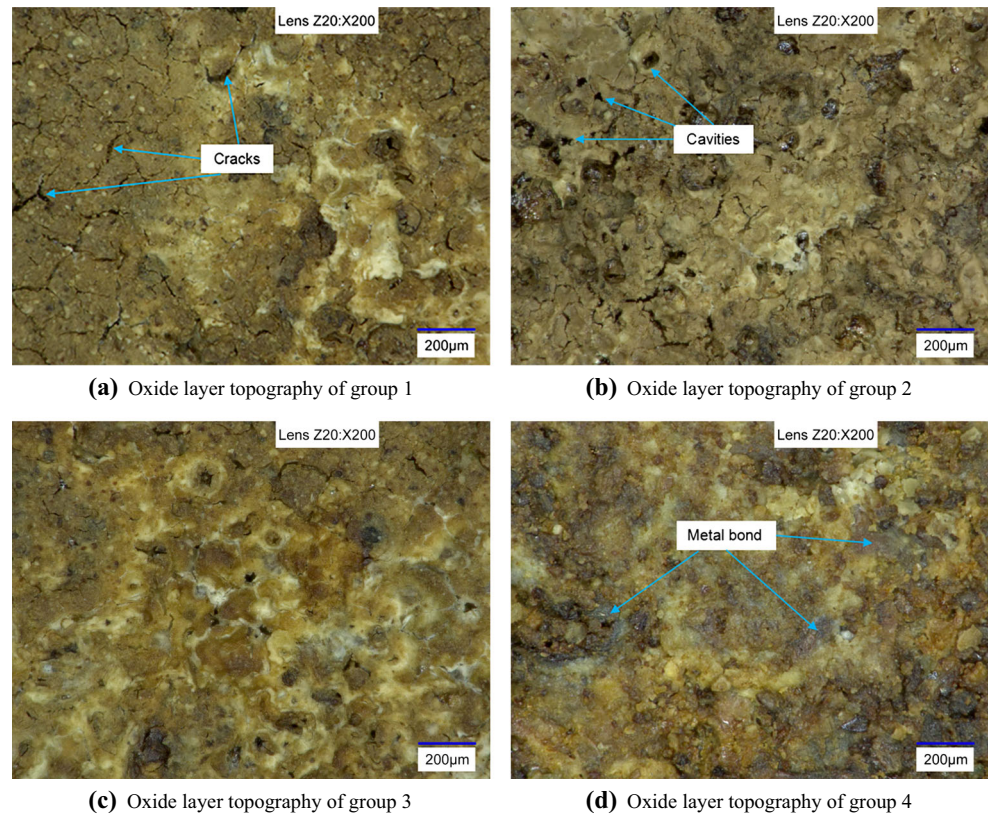
4.3 Topography of oxide layer on the surface of the grinding wheel

Uniform and smooth oxide layer can efficiently improve workpiece surface quality in UAEI grinding process. The oxide layer dissolution from metal bond fall off under the

Fig. 11 Surface micro topography of machined workpieces under processing conditions

(a) SEM photograph of group 1

(b) SEM photograph of group 2

(c) SEM photograph of group 3

(d) SEM photograph of group 4

Fig. 12 Topography of oxide
layer on different conditions

(a) Oxide layer topography of group 1

(b) Oxide layer topography of group 2

(c) Oxide layer topography of group 3

(d) Oxide layer topography of group 4

influence of reaction force of workpieces and longitudinal
vibration of wheels, which leads to the constant changes in
the actual grinding depth, material removal mode, and work-
piece surface quality. Thus, the processing condition in each
group could be judged in terms of topography of oxide layer
used to determine the effectiveness of the mathematical
control model of UAEI grinding.

Figure 12 shows the topographies of oxide layer on the
surface of the wheel with different processing conditions.
The cracks and cavities in group 1 are fine and uniform.
The oxide layer is in mound-like shape with nonuniform
cavities in group 2. Only uniform cavities and almost no
micro cracks in group 3. The wheel in group 4 has nonuni-
formly distributed oxide layer with metal bond exposed to
the surface. It is obvious that the surface morphology of the
oxide layer generated by machining parameters calculated
by the model is beneficial to improving the surface quality
of the machined workpiece, proving the effectiveness of the
mathematical control model of UAEI grinding.

The reason for the morphology generation of oxide layer
in group 2 is that the oxide layer is too thick under the strong
electrolytic action. When the adhesive force of abrasive
grains is smaller than the reaction force of the workpiece,
some grains fall off, carrying away part of the oxide layer.
The actual size and distribution of the abrasive grains are
not absolutely uniform, leaving dome shaped holes on the
surface of oxide layer.

5 Conclusions

This study presents a precise and efficient method named
UAEI grinding, which offers a unique, beneficial grinding
wheel condition that is not obtainable by either of the con-
stituent processes when applied independently. According
to the ultrasonic vibration grinding principle and the elec-
trochemical principle, the mathematical control model of
UAEI grinding is established with the purpose to maintain
the constant grain protrusion height. The model is sim-
ulated and experimentally verified at different processing
parameters. The following conclusions are obtained:

1. There exist the positive correlation between average
   current (I_a) and ultrasonic frequency (f), wheel speed
   (v_s) or workpiece speed (v_w), and the negative corre-
   lation between average current (I_a) and grinding ratio
   (G).
2. The control target is keeping abrasive wear rate and
   electrolytic removal rate equal. With the help of the
   mathematical control model of UAEI grinding, this
   target can be realized by adjusting the electrical param-
   eters and the processing parameters.
3. To determine the effectiveness of the mathematical
   control model of UAEI grinding, two groups of process-
   ing parameters determined by the mathematical control
   model and two other groups of specified processing

parameters are adopted to process ZTA ceramics with same specification. The processing conditions can be judged objectively based on grinding force ratio, workpiece surface roughness, workpiece surface microstructure and oxide layer morphology. The experimental results showed that (1) the surface roughness of workpiece can research 0.0487 μm, (2) the grinding force ratio maintains relatively stable, (3) the surface microtopography of workpiece becomes smoother, and (4) the cracks and cavities on the surface of oxide layer are fine and uniform during UAEI dynamic grinding process. Model determined parameters outperform the artificial determined parameters. Overall, the mathematical control model of the UAEI grinding is effective as confirmed by experiment evaluation.

References

1. Bokhan YI, Bulavin VA, Klubovich VV, Sakevich VN, Trofimovich LI (1996) Mechanical properties of structural ceramics based on Al_2O_3. Glass Ceram 53(7-8):240–242
2. Medvedovski E (2001) Wear-resistant engineering ceramics. Wear 249(9):821–828
3. Kapustina TP (1959) The grinding of ceramic materials with free abrasive. Glass Ceram 16(6):323–327
4. Kapustina TP, Bykova AA (1995) The grinding of ceramic material with bonded abrasive. Glass Ceram 16(7):371–375
5. Piskunov EG, Korolev DI (1993) Polishing of the working surfaces of ceramic parts. Refract Ind Ceram 34(5):342–344
6. Ramesh K, Yeo SH, Gowri S, Zhou L (2001) Experimental Evaluation of Super High-Speed Grinding of Advanced Ceramics. Int J Adv Manuf Technol 17(2):87–92
7. Zaitsev GN, Nikitkov NV, Buturovich IK (1980) Effectiveness of surface ultrasonic grinding of ceramics with diamond disks. Glass Ceram 37(4):185–186
8. Azarhoushang B, Tawakoli T (2011) Development of a novel ultrasonic unit for grinding of ceramic matrix composites. Int J Adv Manuf Technol 57(9):945–955
9. Ding K, Fu Y, Su H, Xu H, Cui F, Li Q (2016) Experimental studies on matching performance of grinding and vibration parameters in ultrasonic assisted grinding of SiC ceramics. Int J Adv Manuf Technol doi:10.1007/s00170-016-8977-6
10. Yan YY, Zhao B, Liu JL (2009) Ultraprecision surface finishing of nano-ZrO_2 ceramics using two-dimensional ultrasonic assisted grinding. Int J Adv Manuf Technol 43(5):462–467
11. Wei S, Zhao H, Jing J, Liu Y (2015) Investigation on surface micro-crack evaluation of engineering ceramics by rotary ultrasonic grinding machining. Int J Adv Manuf Technol 81(1):483–492
12. Mamalis AG, Kundark J, Gyani K, Horvath M (2002) On the Precision Grinding of Advanced Ceramics. Int J Adv Manuf Technol 20(4):255–258
13. Kim JD, Lee ES (1996) A Study of Mirror-like Grinding of Fine Ceramics with In-process Electrolytic Dressing. Int J Adv Manuf Technol 12(4):246–254
14. Zhang C, Ohmori H, Marinescu I, Kato T (2001) Grinding of Ceramic Coatings with Cast Iron Bond Diamond Wheels. A Comparative Study: ELID and Rotary Dresser. Int J Adv Manuf Technol 18(8):545–552
15. Murali MS (2014) Hybrid machining processes. In: Nee AYC (ed) Handbook of manufacturing engineering and technology. Springer, London, pp 1–16
16. Lian HS, Guo ZN, Liu JW, Huang ZG, He JF (2016) Experimental study of electrophoretically assisted micro-ultrasonic machining. Int J Adv Manuf Technol 85(9):2215–2124
17. Dubey AK, Shan HS, Jian NK (2008) Analysis of surface roughness and out-of-roundness in the electro-chemical honing of internal cylinders. Int J Adv Manuf Technol 38(5):491–500
18. Lim HS, Fathima K, Kumar AS, Rahman M (2002) A fundamental study on the mechanism of electrolytic in-process dressing (ELID) grinding. Int J mach Tools Manuf 42(8):935–943
19. Yang L, Ren C, Jin X (2010) Experimental study of ELID grinding based on the active control of oxide layer. J Mater Process Technol 210(13):1748–1753
20. Guan JL, Guo DM, Yuan ZJ (2000) Research on the characteristic and roles of oxide film on grinding wheel of flid mirror surface. Chin J Mech Eng 36(5):89–92
21. Nadolny K (2015) Wear phenomena of grinding wheels with sol-Cgel alumina abrasive grains and glassCceramic vitrified bond during internal cylindrical traverse grinding of 100Cr6 steel. Int J Adv Manuf Technol 77(1):83–98
22. Li BM, Zhao B (2003) Modern grinding technology. Mechanical Industry, Beijing
23. Zhang JH (2008) Predict one-way plane grinding hardening layer and research on friction and wear performance. Dissertation, Shandong University
24. Lawn B, Wilshaw R (1975) Indentation fracture: principles and applications. J Mater Sci 10(6):1049–1081
25. Shi XK, Teng L, LI YQ (1996) Critical conditions for brittleness-ductility transition of hard brittle materials. Aviat Precis Manuf Technol 32(4):10–13
26. George J, Peter G (1985) Microindentation analysis of di-ammonium hydrogen citrate single crystals 20(9):3150–3156
27. Yu XG (2004) Micro-fracture mechanism of nano-composite ZTA ceramic research. Dissertation, Shandong University
28. Sairam S, Clifton RJ (1994) Pressure-shear impact investigation of dynamic fragmentation and flow of ceramics. IEEE 21:217–222
29. Marshall DB, Lawn BR, Evans AG (1982) Elastic/plastic indentation damage in ceramics: the lateral crack system 63(11):574–581
30. Kwak JS, Ha MK (2002) Evaluation of wheel life by grinding ratio and static force. J Mech Sci Technol 16(9):1072–1077